Journal of the European Ceramic Society 42 (2022) 5164–5171

Contents lists available at ScienceDirect

Journal of the European Ceramic Society

journal homepage: www.elsevier.com/locate/jeurceramsoc

Short communication

Processing-dependent stabilization of a dissimilar rare-earth boride in high-entropy $(Ti_{0.2}Zr_{0.2}Hf_{0.2}Ta_{0.2}Er_{0.2})B_2$ with enhanced hardness and grain boundary segregation

Mingde Qin [a,b], Sashank Shivakumar [a,b], Tianjiao Lei [c,d], Joshua Gild [a,b], Esther C. Hessong [c,d], Haoren Wang [a,b], Kenneth S. Vecchio [a,b], Timothy J. Rupert [c,d], Jian Luo [a,b,*]

[a] Program of Materials Science and Engineering, University of California San Diego, La Jolla, CA 92093, USA
[b] Department of NanoEngineering, University of California San Diego, La Jolla, CA 92093, USA
[c] Department of Mechanical and Aerospace Engineering, University of California Irvine, Irvine, CA 92697, USA
[d] Department of Materials Science and Engineering, University of California Irvine, Irvine, CA 92697, USA

ARTICLE INFO

Keywords:
High-entropy ceramics
High-entropy borides
Rare-earth borides
Reactive sintering
Borocarbothermal reduction
Hardness
Grain boundary segregation

ABSTRACT

This study demonstrates that 20% of a rare-earth (RE) diboride (ErB_2) can be stabilized in a high-entropy transition metal (TM) diboride, despite the dissimilar chemical properties of RE and TM elements and large differences in lattice parameters of ErB_2 and typical TMB_2. However, the phase formation depends on the fabrication route, which is a noteworthy observation. Specifically, single-phase $(Ti_{0.2}Zr_{0.2}Hf_{0.2}Ta_{0.2}Er_{0.2})B_2$ is synthesized via reactive spark plasma sintering (SPS) using elemental boron and metal elements. In contract, a specimen made by borocarbothermal reduction of binary oxides and SPS possess significant amounts of two Er-rich secondary phases. Notably, the RE addition in high-entropy TM diboride leads to improved hardness. Aberration-corrected scanning transmission electron microscopy (AC STEM) and energy-dispersive X-ray spectroscopy (EDS) elemental analyses further reveal significant Er segregation at grain boundaries. This work suggests that high-entropy ceramics can have significant solubilities of dissimilar components that may enable new, tunable, and improved properties.

1. Introduction

The research on high-entropy materials took off since the independent studies by Yeh et al. [1] and Canter et al. [2] on transition metal (TM) high-entropy alloys (HEAs) in 2004. As the ceramic counterparts to metallic HEAs, various high-entropy ceramics (HECs) have been fabricated in bulk form, including various high-entropy oxides [3–7], borides [8–12], carbides [13–15], and silicides [16–18]. These HECs have been demonstrated to possess superior and sometimes unexpected properties when compared with their components [5,19,20]. In 2020, it was further proposed to broaden HECs to compositionally complex ceramics (CCCs), where non-equimolar ceramics can outperform their high-entropy counterparts (e.g., in their thermomechanical properties) [5,21,22] and various long- and short-range orders can be further introduced [6,7,17,23].

Among the HECs, high-entropy borides [12], carbides [15,24], and nitrides [25,26] have been extensively studied as a new type of ultrahigh temperature ceramics (UHTCs) due to their potential ability to withstand extreme environments in nuclear and aerospace engineering applications [27]. Particularly, Gild et al. [12] synthesized $(Ti_{0.2}Zr_{0.2}Hf_{0.2}Ta_{0.2}Nb_{0.2})B_2$ and five other single-phase high-entropy diborides (HEDBs) from binary diborides in hexagonal AlB_2-typed structure in 2016, which were the first non-oxide HECs synthesized in bulk form. These HEDBs have been demonstrated to possess improved hardness and oxidation resistance going beyond the simple mixture effect of each component. Since then, more fabrication routes, involving borocarbothermal reduction of metal oxides [18,28] and reactive sintering of elemental powders [29], have been developed to synthesize dense HEDBs. Dual-phase high-entropy UHTCs have also been fabricated [30]. Notably, Qin et al. [29] successfully incorporated Mo and W into HEDBs via reactive spark plasma sintering (SPS) of elemental powders after high-energy ball milling (HEBM). A similar method has

* Corresponding author at: Department of NanoEngineering; Program of Materials Science and Engineering, University of California San Diego, La Jolla, CA 92093, USA.
E-mail address: jluo@alum.mit.edu (J. Luo).

https://doi.org/10.1016/j.jeurceramsoc.2022.05.034
Received 6 April 2022; Received in revised form 13 May 2022; Accepted 15 May 2022
Available online 18 May 2022

been adopted to fabricate high-entropy monoborides [9,31], M_3B_4 borides [11], as well as a broader content of rare earth (RE) high-entropy tetraborides [10] and hexaborides [8]. In other studies, RE high-entropy hexaborides have also been synthesized via the route of borocarbothermal reduction [32,33], together with the composites containing borates [33] or tetraborides [34]. It is well-known that RE elements have the ability to form stable boride compounds at a much wider range of metal-to-boron stoichiometric ratio, from AlB_2-typed diborides to YB_{66}-typed hectoborides [35]; hence, it inspires us to further explore novel high-entropy borides containing RE elements. Specifically, the ability to adding RE in high-entropy TM diborides may enable new opportunities to engineer their oxide scales.

Diborides of AlB_2-prototype have been widely discovered in RE elements, including Sc, Y, Sm, Gd, Tb, Dy, Ho, Er, Tm, Yb and Lu, as summarized in earlier handbooks [35,36]. These RE diborides have the same structure as TM diborides, but with noticeably larger lattice parameters than typical TM diborides [35,36]. Moreover, they feature a unique paramagnetic-to-ferromagnetic transition at low temperature (<150 K) [35,36]. Nevertheless, the RE diborides still remain less studied because they are extremely difficult to prepare in single-phase form. Conventional synthesis routes from elemental precursors usually requires extremely high static pressure (6–7 GPa) aided by high temperature (>1000 °C) [35], and common impurities involve tetraborides, oxides, as well as unreacted metals [37,38].

Here, we hypothesize that HECs can have more solubilities of dissimilar components (with normally less mutual solubilities). To test this hypothesis, this study demonstrates that 20% of a RE diboride (ErB_2) can be stabilized in a high-entropy TM diboride, despite the dissimilar chemical properties of RE and TM elements and large differences in lattice parameters of ErB_2 and typical TMB_2 (or the radii of RE and TM). Unfortunately, the solid solubility of ErB_2 and typical TMB_2 (TM = Zr, Hf, Ti, Ta, and Nb) has not been reported, while we suspect the low solid solubility given the large difference in atomic and ionic radii and dissimilar chemical properties based on the famous Hume-Rothery rules. In this study, we investigate two independent routes (viz. boron-metals reactive SPS of elemental powders and borocarbothermal reduction of oxides followed by SPS) to synthesize a novel RE-containing HEDB with nominal composition of $(Ti_{0.2}Zr_{0.2}Hf_{0.2}Ta_{0.2}Er_{0.2})B_2$. The specimen synthesized via boron-metals reactive SPS demonstrates a perfect single-phase AlB_2-typed structure without measurable impurity. Furthermore, this novel HEDB with 20% Er features enhanced hardness compared to typical $(Ti_{0.2}Zr_{0.2}Hf_{0.2}Ta_{0.2}Nb_{0.2})B_2$ HEDB, even though ErB_2 is predicted to be much softer by itself [53–55]. Moreover, Er (with the lattice parameters of ErB_2 larger than those of typical TM diborides) has been revealed to exhibit significant segregation along grain boundaries in $(Ti_{0.2}Zr_{0.2}Hf_{0.2}Ta_{0.2}Er_{0.2})B_2$ specimen.

In general, this study suggests a new paradigm by showing that HECs can enable enhanced solubility of dissimilar cations. Subsequently, it provides new opportunities to tailor their mechanical properties (e.g., improvement of hardness or impediment of high-temperature dislocation motion due to lattice distortion) and grain boundary properties (e.g., via the expected strong segregation that can significantly change grain growth and grain boundary mechanical properties).

2. Experimental

Specimens with the same nominal composition $(Ti_{0.2}Zr_{0.2}Hf_{0.2}Ta_{0.2}Er_{0.2})B_2$ were synthesized via two different routes: (1) reactive SPS from elemental (boron + metals) precursors, and (2) borocarbothermal reduction of binary metal oxides followed by SPS. For the first route of boron-metals reactive SPS, elemental powders of Ti, Zr, Hf, Ta (>99% purity, ~325 mesh, purchased from Alfa Aesar, MA), Er (99.9% purity, ~40 mesh, purchased from Alfa Aesar, MA), and B (99% purity, 1–2 μm, purchased from US Research Nanomaterials, TX) were utilized as precursors. Stoichiometric amounts of elemental powders were weighed out in batches of 5 g, together with 3 at% of additional boron (i.e., a nominal metal-to-boron atomic ratio of 1: 2.06) to compensate for boron loss in the reaction with the native oxide [29,39] and to minimize the formation of secondary borides [10,30]; moreover, 1 wt% (0.05 g) of stearic acid was added as lubricant for each batch of powder mixture. The powders were first mixed by a vortex mixer, and successively transferred into a tungsten carbide (WC) lined stainless steel milling jar with 11.2 mm diameter WC milling media (at ball-to-powder ratio of ~4.5:1) then high-energy ball milled (HEBM) in a SPEX 8000D mill (SPEX CertiPrep, NJ) for 50 min. The as-milled powders were subsequently loaded into 10 mm graphite dies lined with graphite foils in batches of 2.5 g, and sintered into dense pellets in vacuum (10^{-2} Torr) using a Thermal Technology 3000 series SPS (Thermal Technology LLC, CA) at a final densification temperature of 1950 °C for 10 min. The optimized SPS heating profile can be found in a prior publication [29], where the specimens were first isothermally held at 1400 and 1600 °C before the final densification. It should also be noted that the HEBM and the successive handling of the as-milled powders were conducted in an argon atmosphere (O_2 < 10 ppm) to prevent oxidation.

For the second route of borocarbothermal reduction followed by SPS, binary metal powders of TiO_2, ZrO_2, HfO_2, Ta_2O_5 (>99% purity, ≥ 45 μm, purchased from Alfa Aesar, MA), and Er_2O_3 (99.9% purity, 5 μm, purchased from US Research Nanomaterials, TX), as well as B_4C (99.9% purity, 1–3 μm, purchased from US Research Nanomaterials, TX) were utilized as precursors. Appropriate amounts of precursors were weighted out in batches of 10 g to formulate the target composition of $(Ti_{0.2}Zr_{0.2}Hf_{0.2}Ta_{0.2}Er_{0.2})B_2$ via nominal chemical reaction $14TiO_2 + 14ZrO_2 + 14HfO_2 + 7Ta_2O_5 + 7Er_2O_3 + 50B_4C \rightarrow 70(Ti_{0.2}Zr_{0.2}Hf_{0.2}Ta_{0.2}Er_{0.2})B_2 + 30B_2O_3 + 50CO$. Similarly, 20 mol.% of excess B_4C (i.e., an actual stoichiometric number of $60B_4C$ in the reaction above) was added into the mixture to fully consume the metal oxides and to minimize remaining B_4C as well as metal carbide formation [18,40]. The borocarbothermal reduction and the subsequent SPS followed the procedure originally developed in a prior study [18]: the mixture powders were first planetary ball milled in a PQN04 mill (Across International LLC, NJ), then loaded into a Red Devil graphite furnace (R.D. Webb, MA) and annealed at 1550 °C for 90 min in vacuum (~10^{-4} bar) for borocarbothermal reduction, and finally densified in the SPS at 2000 °C for 30 min. Ref. [18] provides additional experimental details.

After SPS, specimens with the same nominal composition $(Ti_{0.2}Zr_{0.2}Hf_{0.2}Ta_{0.2}Er_{0.2})B_2$ synthesized via two different routes were ground and successively polished for further characterization. X-ray diffraction (XRD) spectra were obtained from a Miniflex II diffractometer (Rigaku, Japan) at 30 kV and 15 mA. Scanning electron microscopy (SEM), energy dispersive X-ray spectroscopy (EDS) and electron backscatter diffraction (EBSD) data were acquired in an Apreo microscope (Thermo Fisher Scientific, MA) equipped with Oxford N-Max^N EDS detector and an Oxford Symmetry EBSD detector. For the specimen synthesized via reactive SPS, bulk density was measured by Archimedes' method, the lattice parameters were determined by XRD unit cell refinement, and its theoretical density was calculated based on lattice parameters and the composition measured by SEM-EDS.

Vickers microhardness measurement was carried out by a Duramin-40 automatic hardness tester (Struers, DK) with indentation loads between 0.49 N (50 gf) and 9.8 N (1 kgf) and dwell time of 10 s abiding by ASTM C1327–15. Over 50 valid measurements were conducted at each indentation load to ensure the statistical accuracy and minimize the surface morphology effects.

Scanning transmission electron microscopy (STEM) samples were fabricated by using the focused ion beam (FIB) lift-out method with a Ga+ ion beam in an FEI Quanta 3D FEG dual-beam SEM/FIB microscope equipped with an OmniProbe. High-angle annular dark-field (HAADF) STEM-EDS were performed to study the grain boundary chemistry, by using a JEOL JEM-ARM300F Grand ARM STEM with double Cs correctors operated at 300 kV. A probe current of 115 pA was used. For HAADF-STEM imaging, the camera length was 6 cm, with the corresponding inner and outer collection angles being 106 and 180 mrad,

respectively.

3. Results and discussion

XRD spectra of $(Ti_{0.2}Zr_{0.2}Hf_{0.2}Ta_{0.2}Er_{0.2})B_2$ specimens synthesized via boron-metals reactive SPS and borocarbothermal reduction followed by SPS are illustrated in Fig. 1(a) and (b), respectively. For the fabrication route of boron-metals reactive SPS, the measured XRD spectrum of the as-milled powder mixture (after HEBM) and the corresponding calculated XRD spectrum for an AlB_2-typed $(Ti_{0.2}Zr_{0.2}Hf_{0.2}Ta_{0.2}Er_{0.2})B_2$ solid solution, assuming random cation occupation and grain orientation, are also shown in Fig. 1(a). After HEBM, the as-milled powder mixture of six elemental precursors demonstrates multiple distinct BCC (Ti, Zr, Hf, and Ta) and HCP (Er) phases in Fig. 1(a). This implies that the reaction between boron and metals, as well as the formation of high-entropy solid solution, takes place during the following SPS (not the preceding HEBM). The peak broadening observed in this spectrum can be associated with grain size reduction, lattice distortion, and micro-strains that are commonly induced by HEBM. For the sintered pellet after reactive SPS, however, the XRD spectrum exhibits a perfect single phase of hexagonal AlB_2-prototype without any detectable secondary phase or impurity. Interestingly, in this XRD spectrum of sintered pellet, asymmetric peak broadening has been observed for all planes that intercept *c*-axis ([001] direction), i.e., (001), (101), (002), etc.; in contrast, no obvious asymmetry has been recognized for diffraction peaks corresponding to the planes that are parallel to *c*-axis. This could relate to the layered structure of AlB_2-typed solid solution, where the interplanar distance along *c*-axis depends more on large components [12,29]. In $(Ti_{0.2}Zr_{0.2}Hf_{0.2}Ta_{0.2}Er_{0.2})B_2$ solid solution, ErB_2 has significantly larger lattice parameters ($a = 3.261$ Å, $c = 3.779$ Å) [41] than the other TMB_2 components, viz. TiB_2 ($a = 3.031$ Å, $c = 3.237$ Å) [42], ZrB_2 ($a = 3.168$ Å, $c = 3.531$ Å) [43], HfB_2 ($a = 3.142$ Å, $c = 3.477$ Å) [43], and TaB_2 ($a = 3.097$ Å, $c = 3.226$ Å) [43], and the expanded lattice (by larger ErB_2) has induced considerable tensile lattice strain, especially along *c*-axis, with the existence of other smaller components, which further engenders the asymmetric peak broadening towards the high-angle side for planes that intercept *c*-axis ([001] direction).

In contrast to the single-phase specimen by boron-metals reactive SPS, the specimen with the same nominal composition synthesized via borocarbothermal reduction of binary oxides followed by SPS demonstrates a major diboride phase with substantial amounts of secondary phases in Fig. 1(b), and these secondary phases have been revealed to be Er-rich (by EDS analysis in Fig. 2(d)), and they can be further identified as $ErBO_3$- and ErB_4-based solid solutions by the XRD spectrum. RE borate is an intermediate phase during the borocarbothermal reduction which can be found in RE boride systems, following the nominal reaction $4RE_2O_3 + 3B_4C \rightarrow 4REBO_3 + 4REB_2 + 3\,C$, when binary oxides are not fully reduced [33]; on the other hand, RE tetraborides can also be reduced from binary oxides, complying with the equation $7RE_2O_3 + 15B_4C \rightarrow 14REB_4 + 2B_2O_3 + 15CO$, and have been reported from raw materials with lower oxide contents [34]. In fact, borocarbothermal reduction of RE binary oxides is a rather complicated process with intermediate phases and boride products of different RE valence states; hence, the existence of the secondary phases is anticipated. The content of these secondary phases may be reduced (or even eliminated) at optimized reduction conditions (e.g., oxide-to-reductant ratio, reduction temperature and time, etc.).

SEM micrographs of the polished surface in Fig. 2(a) illustrates that the specimen made by reactive SPS is highly dense (<1% porosity); in fact, this specimen exhibits an exceptional relative density of 99.1% by comparing its experimentally measured bulk density (8.74 g/cm^3) with the theoretically calculated density (8.82 g/cm^3). Moreover, this specimen also manifests a largely homogenous solid solution without noticeable secondary phase or particles. The SEM-EDS elemental maps in Fig. 2(c) further confirms the unform distributions of its constituent elements. At the same time, quantitative EDS analysis measured a composition of $(Ti_{0.18}Zr_{0.21}Hf_{0.23}Ta_{0.19}Er_{0.19})B_2$, which is within typical EDS measurement errors from the nominal equimolar composition. Hence, the nominal composition is still adopted in the following discussion. We note that tungsten carbide milling media can often cause contamination of tungsten; e.g., a prior study showed 1–5 at% tungsten can be introduced from aggressive HEBM [30]. Nevertheless, tungsten contamination in the specimen made in this study was below the EDS detection limit. We believe that this is due to the following reasons. First, this study used a relatively short the HEBM duration of 50 min (vs. 100 min in the prior study [30]). Second, our precursor powders

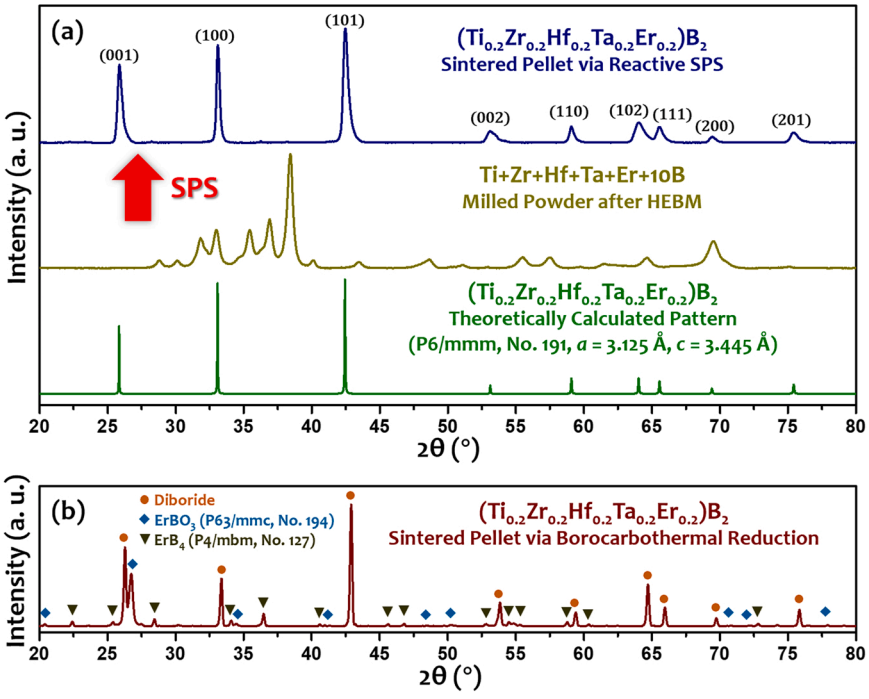

Fig. 1. XRD spectra of $(Ti_{0.2}Zr_{0.2}Hf_{0.2}Ta_{0.2}Er_{0.2})B_2$ specimens synthesized via (a) reactive SPS from elemental precursors and (b) borocarbothermal reduction of binary oxides. In Panel (a), experimental XRD spectra of as-sintered pellet fabricated by metal-boron reactive SPS and as-milled powder mixture (after HEBM) are shown, along with the corresponding calculated XRD spectrum for the $(Ti_{0.2}Zr_{0.2}Hf_{0.2}Ta_{0.2}Er_{0.2})B_2$ solid solution, assuming random cation occupation and grain orientation, for comparison. On the one hand, the specimen fabricated via reactive SPS from elemental precursors demonstrates a single AlB_2-prototyped hexagonal phase without any detectable secondary phase by XRD. On the other hand, specimen with the same nominal composition fabricated via borocarbothermal reduction of binary oxides shows secondary phases from the XRD spectrum, which were shown to be Er-rich (by the EDS analysis) and further identified as $ErBO_3$- and ErB_4-based solid solutions.

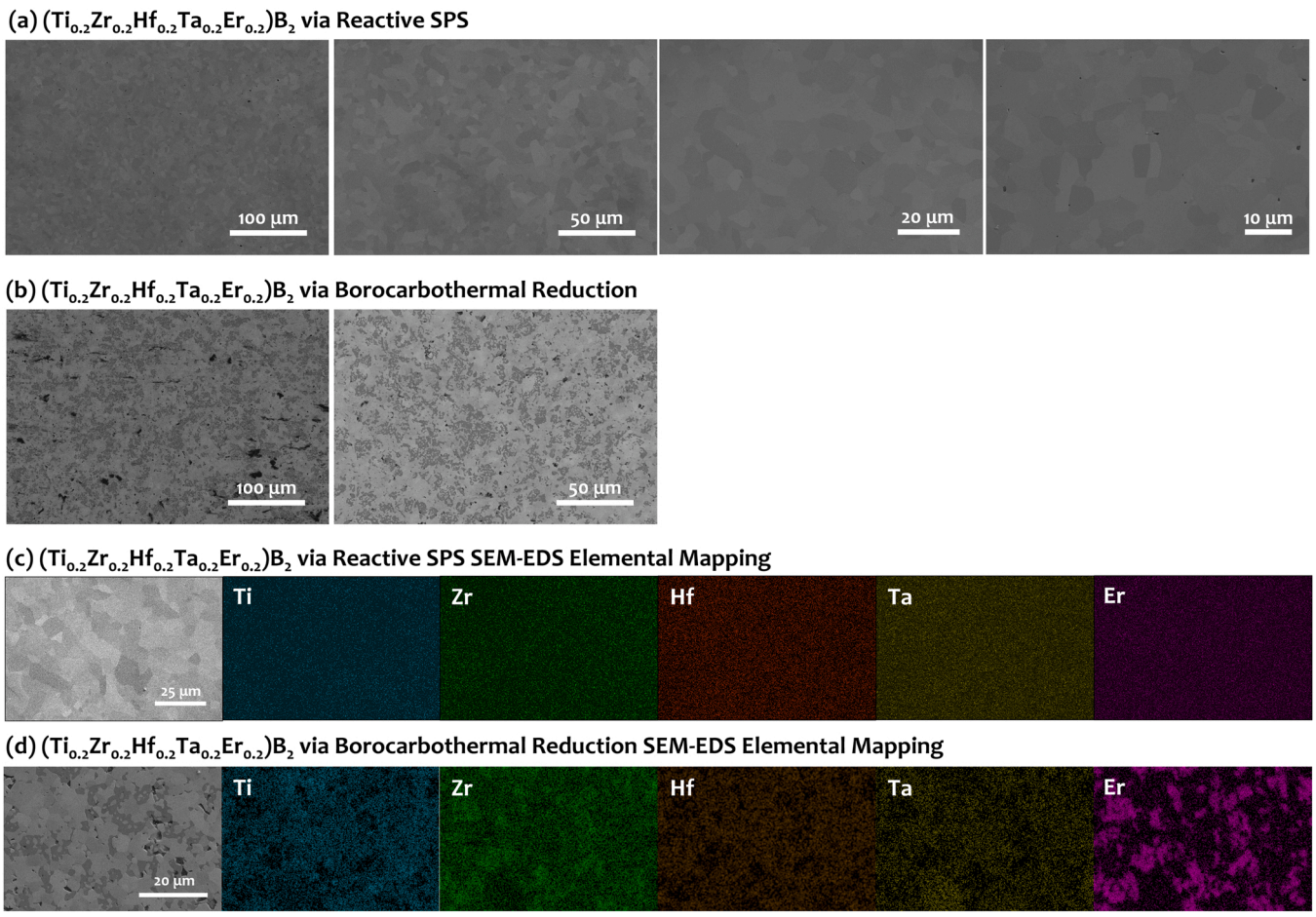

Fig. 2. SEM micrographs at different magnifications and SEM-EDS elemental maps of the $(Ti_{0.2}Zr_{0.2}Hf_{0.2}Ta_{0.2}Er_{0.2})B_2$ specimens synthesized via (a, c) reactive SPS from elemental precursors and (b, d) borocarbothermal reduction of binary oxides. The single-phase $(Ti_{0.2}Zr_{0.2}Hf_{0.2}Ta_{0.2}Er_{0.2})B_2$ specimen synthesized via reactive SPS is homogenous under SEM and all the constituent elements are uniformly distributed. In contrast, the specimen synthesized via borocarbothermal reduction with the same nominal composition possesses multiple phases with different contrasts in the SEM micrographs, and Er-rich regions are evident in the elemental maps. The SEM micrographs of the single-phase specimen synthesized via direct boron-metals reactive SPS are also obtained at high magnifications to illustrate more microstructure details.

(elemental metals and boron) used here are much softer than the binary diborides and carbides mixtures utilized in the previous case [30], which likely resulted in a much lower wear rate of the tungsten carbide jar and balls.

By comparison, the specimen fabricated via borocarbothermal reduction demonstrates multiple distinct phases of different contrasts with considerable amount of porosity (Fig. 2(b)), and SEM-EDS elemental maps in Fig. 2(d) further reveals the Er-rich secondary phases.

The combination of XRD, SEM, and EDS demonstrates that a novel high-entropy RE-containing solid solution of $(Ti_{0.2}Zr_{0.2}Hf_{0.2}Ta_{0.2}Er_{0.2})B_2$ in AlB_2-typed hexagonal structure has been successfully achieved by boron-metals reactive SPS, despite the dissimilar chemical properties of RE and TM elements and large differences in lattice parameters of ErB_2 and typical TMB_2 (or Er and TM radii) aforementioned. This result suggests a new paradigm by showing that HECs can enable significant solubility of dissimilar cations where 20% RE element (Er) can be stabilized in a high-entropy TM diboride.

By comparison, high-entropy solid solution of the same nominal $(Ti_{0.2}Zr_{0.2}Hf_{0.2}Ta_{0.2}Er_{0.2})B_2$ composition was not obtained via borocarbothermal reduction from binary oxides followed by SPS. The existence of Er-rich $ErBO_3$- and ErB_4-based solid solution in the final specimen indicates that the phase formation in $(Ti_{0.2}Zr_{0.2}Hf_{0.2}Ta_{0.2}Er_{0.2})B_2$ depends on the fabrication route where the intermediate RE borate and other stable RE borides can exist in the final product depending on the conditions of borocarbothermal reduction.

EBSD analyses have been carried out the measure the grain size, determine the crystal orientation, and examine the texture for the single-phase $(Ti_{0.2}Zr_{0.2}Hf_{0.2}Ta_{0.2}Er_{0.2})B_2$ specimen, and the results are illustrated in Fig. 3. The grain size has been determined to be 4.49 $\pm$ 1.65 μm, smaller than typical high-entropy TM diborides synthesized at 2000 °C or higher [29,44]. Notably, the specimen features a preferred grain orientation of (001) plane normal to the direction of the SPS pressure and current as illustrated in Fig. 3(a) and (c), which is consistent with other studies on high-entropy TM diborides [29,45] and earlier work on TiB_2 [46,47].

Furthermore, Vickers microhardness measurements have been conducted on this single-phase specimen at full indentation load range from 0.49 N to 9.8 N to systematically examine its hardness (Fig. 4(a)). Similar to other brittle and incompressible materials that are subjected to indentation size effect [48], this specimen demonstrates increasing measured hardness with decreasing indentation load, going from 18.9 $\pm$ 1.4 GPa at 9.8 N to 35.8 $\pm$ 5.5 GPa at 0.49 N. At the same indentation load of 1.96 N, this specimen is noticeably harder than a $(Ti_{0.2}Zr_{0.2}Hf_{0.2}Ta_{0.2}Nb_{0.2})B_2$ specimen synthesized by the same direct boron-metals reactive SPS method with a similar 98.1% relative density (24.4 $\pm$ 2.5 GPa for $(Ti_{0.2}Zr_{0.2}Hf_{0.2}Ta_{0.2}Er_{0.2})B_2$ here vs. 20.9 $\pm$ 1.1 GPa for the reference $(Ti_{0.2}Zr_{0.2}Hf_{0.2}Ta_{0.2}Nb_{0.2})B_2$ [29]), as compared in Fig. 4(b). It is comparable to those so-called "superhard" HEDBs recently made with addition of CrB_2, MoB_2, and/or WB_2 [18,29].

The hardness of the parent TMB_2 phases was measured to be 18.6

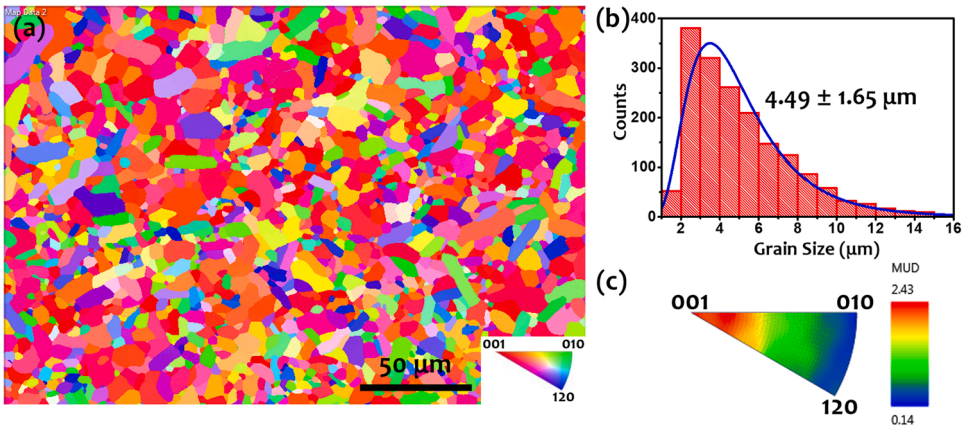

Fig. 3. (a) EBSD normal direction inverse pole figure grain orientation map for $(Ti_{0.2}Zr_{0.2}Hf_{0.2}Ta_{0.2}Er_{0.2})B_2$ specimen synthesized via reactive SPS, as well as the corresponding (b) grain size distribution and (c) inverse pole figure of crystal preferred orientation. In panel (c), the contour maps represent the multiples of uniform distribution (MUD). This specimen features a preferred grain orientation of (001) plane normal to the direction of the SPS pressure and current.

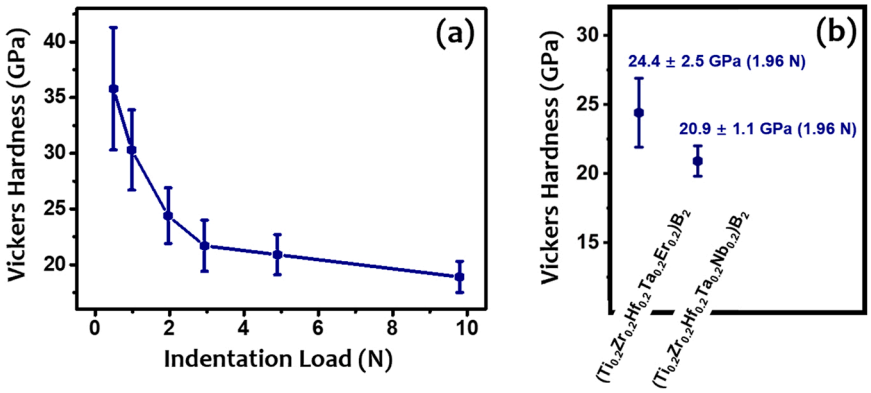

Fig. 4. (a) Measured Vickers microhardness values of the single-phase $(Ti_{0.2}Zr_{0.2}Hf_{0.2}Ta_{0.2}Er_{0.2})B_2$ specimen synthesized via reactive SPS with the indentation loads from 0.49 N (50 gf) to 9.8 N (1 kgf). (b) Comparation of Vickers microhardness values of direct boron-metals reactive SPS synthesized $(Ti_{0.2}Zr_{0.2}Hf_{0.2}Ta_{0.2}Er_{0.2})B_2$ from this study and a reference $(Ti_{0.2}Zr_{0.2}Hf_{0.2}Ta_{0.2}Nb_{0.2})B_2$ specimen made via the same method from a prior study [29], measured at the same indentation load of 1.96 N. It is interesting to further note that ErB_2 is expected to be significantly softer than refractory metal diborides TMB_2 (based on simulations [53–55]). Thus, adding ErB_2 likely increased the hardness of the $(Ti_{0.2}Zr_{0.2}Hf_{0.2}Ta_{0.2}Er_{0.2})B_2$.

$\pm$ 1.3 GPa for HfB_2, 15.4 $\pm$ 1.1 GPa for ZrB_2, 17.5 $\pm$ 10.8 GPa for TaB_2, 25.0 $\pm$ 1.8 GPa for TiB_2, and 15.6 $\pm$ 0.9 GPa for NbB_2, respectively, at the 1.96 N indentation load, but on specimens synthesized by a different (less optimized) method [12]. Because of the different synthesis methods involved (therefore high porosity and oxide inclusion in that prior study [12] that can significantly reduce the hardness), these hardness values cannot be compared with the current study directly. For example, the prior study also synthesized a $(Ti_{0.2}Zr_{0.2}Hf_{0.2}Ta_{0.2}Nb_{0.2})B_2$ with that (less optimized) method and measured its hardness to be 17.5 $\pm$ 1.2 GPa [12] (lower than 20.9 $\pm$ 1.1 GPa measured for a specimen synthesized using the same direct boron-metals reactive SPS method [29] used here). The hardness value of bulk ErB_2 synthesized by the same method has not been measured, but rare earth metal diborides REB_2 are expected to be significantly softer than refractory metal diborides TMB_2 in general (based on simulations [53–55]). Thus, the addition of ErB_2 likely increased the hardness of the HEDB.

To discuss the effects of relative density and grain size, we adopt a e^{-bP} dependence of hardness on porosity (P) [49], with value $b = 1.9$ [50] or 5.5 [51]. This suggests a mere 2–5% increase in hardness when relative density increase from ~98% to ~99%. Moreover, Rice et al. [52] suggests small increase in hardness (<~2%) when grain size decreases from 13 μm to 4.5 μm, but the Hall-Petch dependence of $G^{-0.5}$ on grain size (G) only becomes phenomenal when the grain size is smaller than ~1 μm. Thus, we conclude that relative density and grain size do not play a significant role on the observed enhanced hardness here.

In this instance, it can be concluded that the hardness of HEDB has been noticeably enhanced by addition of 20% RE element, where the large lattice strain induced by the great difference in lattice parameters between ErB_2 and the rest TMB_2 components (discussed above) may have a contribution. Although the hardness of binary ErB_2 has never been experimentally measured to the best of our knowledge, simulation studies have predicted that ErB_2, as well as other RE diborides, have significantly lower hardness than TM diborides [53–55]. Hence, this HEDB, which can attain higher hardness by incorporation of softer REB_2 component, provides another example where HECs can attain unexpected properties beyond what the simple rule of mixtures can predict.

To further explore the elemental distribution near grain boundaries in the single-phase $(Ti_{0.2}Zr_{0.2}Hf_{0.2}Ta_{0.2}Er_{0.2})B_2$ specimen, STEM samples of two independent grain boundaries were prepared and characterized. The locations of these two grain boundary samples were selected randomly from the polished specimen surface to ensure the validity and representative character. Their STEM micrographs, as well as the STEM-EDS results, are shown in Fig. 5. It is obvious that all five elements exhibit very homogenous distributions within the crystal grains. Nevertheless, RE element Er demonstrates significant grain boundary segregation in both samples, as clearly indicated by STEM-EDS mappings (Fig. (a2) and (b2)) and STEM-EDS line-scan profiles (Fig. (a3) and (b3)) over the grain boundaries. Contrarily, depletion of Zr and Hf on the grain boundaries have also been observed, while the contents of Ti and Ta stay relatively constant across the grain boundaries. As ErB_2 has significantly larger lattice parameters than the rest TMB_2 components (see discussion above), this Er segregation on grain boundary can be expected due to lattice mismatch and lattice strain. In fact, grain boundary segregation has also observed in W-containing HEDBs [56], where WB_2 bears smaller lattice than the other TM diboride constituents. Similarly, the Er grain boundary segregation, together with the associated lattice strain and dislocation, could suppress the grain growth

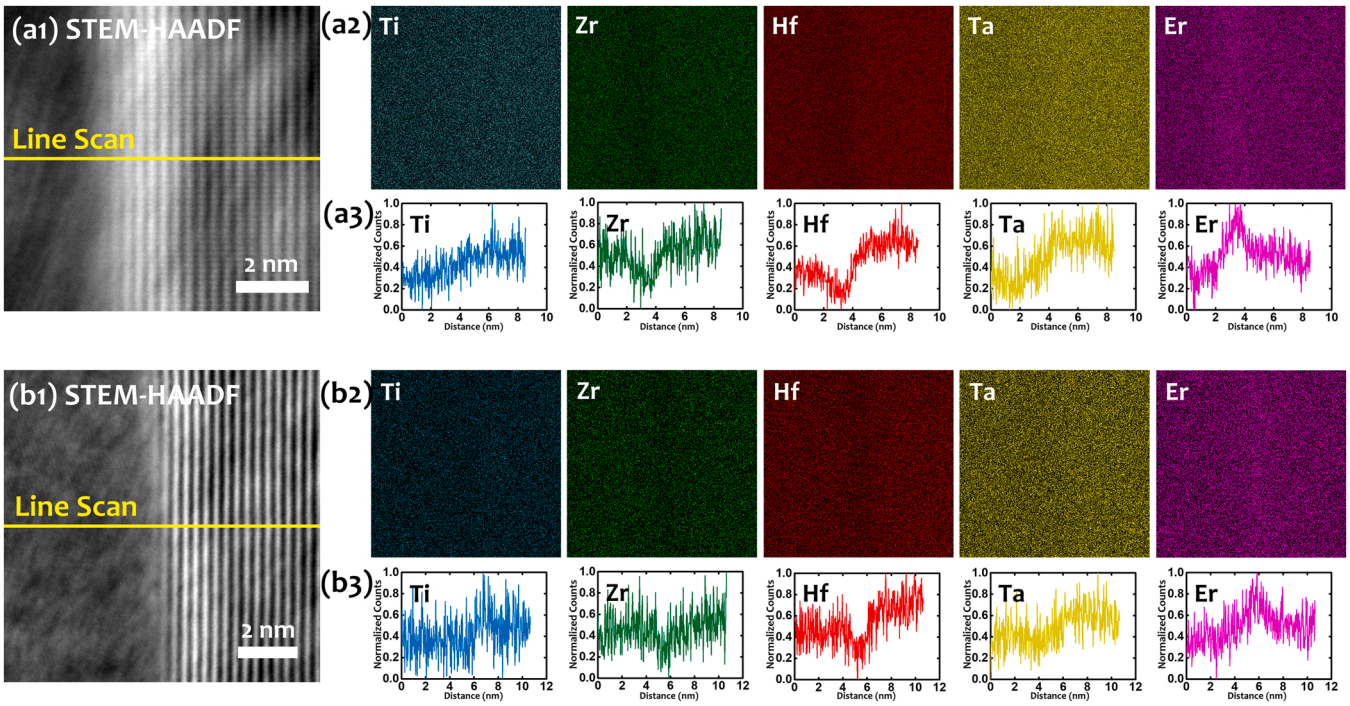

Fig. 5. STEM characterization of two independent grain boundaries of the single-phase $(Ti_{0.2}Zr_{0.2}Hf_{0.2}Ta_{0.2}Er_{0.2})B_2$ specimen synthesized via reactive SPS. The location of these two grain boundaries, (a) and (b), were selected randomly on the polished specimen surface to ensure the validity and representativeness. STEM-HAADF micrographs, (a1) and (b1), illustrate the structures of the grain boundaries at the atomic scale. The corresponding STEM-EDS elemental mappings, (a2) and (b2), demonstrate the elemental distributions around the grain boundaries at the nanoscale. STEM-EDS line-scan profiles, (a3) and (b3), further reveal the elemental distributions across the grain boundaries. Strong Er segregation at grain boundaries is evident.

and contribute to the improvement of material hardness for this $(Ti_{0.2}Zr_{0.2}Hf_{0.2}Ta_{0.2}Er_{0.2})B_2$ HEDB solid solution. It should be pointed out that the enhancement in hardness should be a synergic effect of many factors, and Er grain boundary segregation may not have the dominating influence.

Nonetheless, the ability to dissolve substantial dissimilar metal cations (with large chemical and size mismatches) in HECs suggest new opportunities to tailor grain boundary properties, e.g., via the expected strong segregation that can significantly change grain growth and grain boundary mechanical (e.g., high-temperature sliding) properties. Thus, this may open a new window to engineer grain boundary properties and microstructures of HECs via accommodating a substantial amount of normally less soluble, or even immiscible, cations (components).

To the best of our knowledge, we were not aware of any prior report of RE-containing HEBs during our experiments. In our final manuscript preparation stage, we noticed that parallel work published by Zhang et al. (just a few days before the submission of this manuscript) also successfully synthesized several RE-containing HEDBs (with different compositions as we reported here) [57] and a Sc-containing HEDB [58]. In Zhang et al.'s most recent simultaneous and independent work [57, 58], no property has been measured and reported, and grain boundaries have not been characterized. In addition to the enhanced hardness and strong grain boundary segregation of the RE, another unique observation made in the current study is the fabrication-dependent phase formation.

4. Conclusions

In this study, a novel HEDB containing 20% RE element with nominal composition of $(Ti_{0.2}Zr_{0.2}Hf_{0.2}Ta_{0.2}Er_{0.2})B_2$ has been synthesized via two distinctive routes: boron-metals reactive SPS from elemental precursors and borocarbothermal reduction of binary oxides followed by SPS. The specimen fabricated via borocarbothermal reduction contain Er-rich $ErBO_3$- and ErB_4-based solid solutions. On the other hand, specimen synthesized via boron-metals reactive SPS demonstrates a perfect single-phase high-entropy solid solution of AlB_2-prototype without any detectable impurity or secondary phase. This specimen has an exceptional relative density of 99.1%, and its elemental homogeneity has been verified by SEM-EDS analysis. The successful fabrication of single-phase $(Ti_{0.2}Zr_{0.2}Hf_{0.2}Ta_{0.2}Er_{0.2})B_2$ specimen with 20% RE element (Er) stabilized in a high-entropy TM diborides, despite the dissimilar chemical properties of RE and TM elements and large differences in lattice parameters of ErB_2 and typical TMB_2, suggests a new paradigm by showing that HECs can enable significant solubility of dissimilar cations. Moreover, the existence of borate and secondary boride impurities from borocarbothermal reduction indicates the formation of single-phase $(Ti_{0.2}Zr_{0.2}Hf_{0.2}Ta_{0.2}Er_{0.2})B_2$ depends on the fabrication route. Here, the large thermodynamic driving force in the reactive sintering of elemental precursors may play a key role for incorporating certain components that are otherwise difficult to dissolve in significant amounts.

Notably, with 20% ErB_2 addition, $(Ti_{0.2}Zr_{0.2}Hf_{0.2}Ta_{0.2}Er_{0.2})B_2$ has featured an increase in hardness, in comparison with typical $(Ti_{0.2}Zr_{0.2}Hf_{0.2}Ta_{0.2}Nb_{0.2})B_2$ high-entropy TM diboride, despite the fact that ErB_2 is predicted to be substantially softer. Specific STEM-EDS elemental analyses further revealed significant Er segregation at grain boundaries.

In broader context, the validation of our hypothesis that a substantial amount of dissimilar metal cations (with large chemical and size mismatches) can be stabilized in HECs and CCCs suggest new opportunities to tailor their mechanical properties, e.g., promoting more lattice distortion to improve hardness or impede high-temperature dislocation motion, or grain boundary properties via the expected strong segregation that can alter microstructural evolution (e.g., inhibit grain growth) and high-temperature properties (e.g., grain boundary sliding or preferred grain boundary oxidation). Specifically, for RE-containing HEDBs, in addition to the the enhanced hardness (that has already been demonstrated here), the ability to add a substantial amount of RE

in high-entropy TM diborides opens a new window to tailor their oxidation resistance, including the formation/stability of oxide scales and potentially the grain boundary oxidation resistance with the expected strong RE segregation (since preferred grain boundary oxidation was observed in high-entropy UHTCs [59]).

Declaration of Competing Interest

The authors declare that they have no known competing financial interests or personal relationships that could have appeared to influence the work reported in this paper.

Acknowledgement

This research is primarily supported by the National Science Foundation, USA (NSF) Materials Research Science and Engineering Center Multidisciplinary Universrvine Center for Complex and Active Materials (CCAM) via NSF grant no. DMR-2011967 currently (for 2020–2026). We also acknowledge the earlier support from an Office of Naval Research Multidisciplinary University Research Initiative program (N00014–15-1–2863, for 2015–2020) prior the start of CCAM, particularly for the borocarbothermal reduction fabrication route as our initial trial and benchmark comparison, as well as shared characterization facilities of UCSD NanoEngineering's Materials Research Center (NE-MRC), the San Diego Nanotechnology Infrastructure (SDNI) of UCSD, a member of the National Nanotechnology Coordinated Infrastructure supported by the NSF (ECCS-1542148), UC Irvine Materials Research Institute (IMRI).

References

[1] J.-W. Yeh, S.-J. Lin, T.-S. Chin, J.-Y. Gan, S.-K. Chen, T.-T. Shun, C.-H. Tsau, S.-Y. Chou, Formation of simple crystal structures in Cu-Co-Ni-Cr-Al-Fe-Ti-V alloys with multiprincipal metallic elements, Metall. Mater. Trans. A 35 (8) (2004) 2533–2536.
[2] B. Cantor, I.T.H. Chang, P. Knight, A.J.B. Vincent, Microstructural development in equiatomic multicomponent alloys, Mater. Sci. Eng. A 375–377 (2004) 213–218.
[3] C.M. Rost, E. Sachet, T. Borman, A. Moballegh, E.C. Dickey, D. Hou, J.L. Jones, S. Curtarolo, J.-P. Maria, Entropy-stabilized oxides, Nat. Commun. 6 (2015) 8485.
[4] S. Jiang, T. Hu, J. Gild, N. Zhou, J. Nie, M. Qin, T. Harrington, K. Vecchio, J. Luo, A new class of high-entropy perovskite oxides, Scripta Mater. 142 (2018) 116–120.
[5] A.J. Wright, J. Luo, A step forward from high-entropy ceramics to compositionally complex ceramics: a new perspective, J. Mater. Sci. 55 (2020) 9812–9827.
[6] M. Qin, H. Vega, D. Zhang, S. Adapa, A.J. Wright, R. Chen, J. Luo, 21-Component compositionally complex ceramics: discovery of ultrahigh-entropy weberite and fergusonite phases and a pyrochlore-weberite transition, J. Adv. Ceram. 11 (4) (2022) 641–655.
[7] A.J. Wright, Q. Wang, C. Hu, Y.-T. Yeh, R. Chen, J. Luo, Single-phase duodenary high-entropy fluorite/pyrochlore oxides with an order-disorder transition, Acta Mater. 211 (2021), 116858.
[8] M. Qin, Q. Yan, Y. Liu, H. Wang, C. Wang, T. Lei, K.S. Vecchio, H.L. Xin, T. J. Rupert, J. Luo, Bulk high-entropy hexaborides, J. Eur. Ceram. Soc. 41 (12) (2021) 5775–5781.
[9] M. Qin, Q. Yan, H. Wang, C. Hu, K.S. Vecchio, J. Luo, High-entropy monoborides: towards superhard materials, Scripta Mater. 189 (2020) 101–105.
[10] M. Qin, Q. Yan, H. Wang, K.S. Vecchio, J. Luo, High-entropy rare earth tetraborides, J. Eur. Ceram. Soc. 41 (4) (2021) 2968–2973.
[11] M. Qin, Q. Yan, Y. Liu, J. Luo, A new class of high-entropy M 3 B 4 borides, J. Adv. Ceram. 10 (1) (2021) 166–172.
[12] J. Gild, Y. Zhang, T. Harrington, S. Jiang, T. Hu, M.C. Quinn, W.M. Mellor, N. Zhou, K. Vecchio, J. Luo, High-entropy metal diborides: a new class of high-entropy materials and a new type of ultrahigh temperature ceramics, Sci. Rep. 6 (2016) 37946.
[13] X. Yan, L. Constantin, Y. Lu, J.F. Silvain, M. Nastasi, B. Cui, (Hf0. 2Zr0. 2Ta0. 2Nb0. 2Ti0. 2) C High-Entropy Ceramics with Low Thermal Conductivity, Journal of the American Ceramic Society 101 (2018) 4486–4491.
[14] E. Castle, T. Csanádi, S. Grasso, J. Dusza, M. Reece, Processing and properties of high-entropy ultra-high temperature carbides, Sci. Rep. 8 (1) (2018) 8609.
[15] T.J. Harrington, J. Gild, P. Sarker, C. Toher, C.M. Rost, O.F. Dippo, C. McElfresh, K. Kaufmann, E. Marin, L. Borowski, P.E. Hopkins, J. Luo, S. Curtarolo, D. W. Brenner, K.S. Vecchio, Phase stability and mechanical properties of novel high entropy transition metal carbides, Acta Mater. 166 (2019) 271–280.
[16] J. Gild, J. Braun, K. Kaufmann, E. Marin, T. Harrington, P. Hopkins, K. Vecchio, J. Luo, A high-entropy silicide: (Mo0. 2Nb0. 2Ta0. 2Ti0. 2W0. 2) Si2, J. Materiomics 5 (3) (2019) 337–343.
[17] S. Shivakumar, M. Qin, D. Zhang, C. Hu, Q. Yan, J. Luo, A new type of compositionally complex M5Si3 silicides: Cation ordering and unexpected phase stability, Scripta Mater. 212 (2022), 114557.
[18] J. Gild, A. Wright, K. Quiambao-Tomko, M. Qin, J.A. Tomko, M. Shafkat bin Hoque, J.L. Braun, B. Bloomfield, D. Martinez, T. Harrington, K. Vecchio, P. E. Hopkins, J. Luo, Thermal conductivity and hardness of three single-phase high-entropy metal diborides fabricated by borocarbothermal reduction and spark plasma sintering, Ceram. Int. 46 (5) (2020) 6906–6913.
[19] H. Xiang, Y. Xing, F.-z Dai, H. Wang, L. Su, L. Miao, G. Zhang, Y. Wang, X. Qi, L. Yao, H. Wang, B. Zhao, J. Li, Y. Zhou, High-entropy ceramics: present status, challenges, and a look forward, J. Adv. Ceram. 10 (3) (2021) 385–441.
[20] S. Akrami, P. Edalati, M. Fuji, K. Edalati, High-entropy ceramics: review of principles, production and applications, Mater. Sci. Eng. R: Rep. 146 (2021), 100644.
[21] A.J. Wright, Q. Wang, C. Huang, A. Nieto, R. Chen, J. Luo, From high-entropy ceramics to compositionally-complex ceramics: a case study of fluorite oxides, J. Eur. Ceram. Soc. 40 (5) (2020) 2120–2129.
[22] A.J. Wright, Q. Wang, S.-T. Ko, K.M. Chung, R. Chen, J. Luo, Size disorder as a descriptor for predicting reduced thermal conductivity in medium- and high-entropy pyrochlore oxides, Scripta Mater. 181 (2020) 76–81.
[23] D. Zhang, Y. Chen, T. Feng, D. Yu, K. An, R. Chen, J. Luo, Discovery of a reversible redox-induced order-disorder transition in a 10-component compositionally complex ceramic, Scripta Mater. 215 (2022), 114699.
[24] P. Sarker, T. Harrington, C. Toher, C. Oses, M. Samiee, J.-P. Maria, D.W. Brenner, K.S. Vecchio, S. Curtarolo, High-entropy high-hardness metal carbides discovered by entropy descriptors, Nat. Commun. 9 (1) (2018) 4980.
[25] T. Jin, X. Sang, R.R. Unocic, R.T. Kinch, X. Liu, J. Hu, H. Liu, S. Dai, Mechanochemical-assisted synthesis of high-entropy metal nitride via a soft urea strategy, Adv. Mater. 30 (23) (2018), 1707512.
[26] O.F. Dippo, N. Mesgarzadeh, T.J. Harrington, G.D. Schrader, K.S. Vecchio, Bulk high-entropy nitrides and carbonitrides, Sci. Rep. 10 (1) (2020) 21288.
[27] W.G. Fahrenholtz, G.E. Hilmas, Ultra-high temperature ceramics: materials for extreme environments, Scripta Mater. 129 (2017) 94–99.
[28] Y. Zhang, Z.-B. Jiang, S.-K. Sun, W.-M. Guo, Q.-S. Chen, J.-X. Qiu, K. Plucknett, H.-T. Lin, Microstructure and mechanical properties of high-entropy borides derived from boro/carbothermal reduction, J. Eur. Ceram. Soc. 39 (13) (2019) 3920–3924.
[29] M. Qin, J. Gild, H. Wang, T. Harrington, K.S. Vecchio, J. Luo, Dissolving and stablizing soft WB2 and MoB2 phases into high-entropy borides via boron-metals reactive sintering to attain higher hardness, J. Eur. Ceram. Soc. 40 (12) (2020) 4348–4353.
[30] M. Qin, J. Gild, C. Hu, H. Wang, M.S.B. Hoque, J.L. Braun, T.J. Harrington, P. E. Hopkins, K.S. Vecchio, J. Luo, Dual-phase high-entropy ultra-high temperature ceramics, J. Eur. Ceram. Soc. 40 (15) (2020) 5037–5050.
[31] P. Zhao, J. Zhu, Y. Zhang, G. Shao, H. Wang, M. Li, W. Liu, B. Fan, H. Xu, H. Lu, Y. Zhou, R. Zhang, A novel high-entropy monoboride (Mo0.2Ta0.2Ni0.2Cr0.2W0.2)B with superhardness and low thermal conductivity, Ceram. Int. 46 (17) (2020) 26626–26631.
[32] H. Chen, Z. Zhao, H. Xiang, F.-Z. Dai, J. Zhang, S. Wang, J. Liu, Y. Zhou, Effect of reaction routes on the porosity and permeability of porous high entropy (Y0.2Yb0.2Sm0.2Nd0.2Eu0.2)B6 for transpiration cooling, J. Mater. Sci. Technol. 38 (2020) 80–85.
[33] W. Zhang, B. Zhao, H. Xiang, F.-Z. Dai, S. Wu, Y. Zhou, One-step synthesis and electromagnetic absorption properties of high entropy rare earth hexaborides (HE REB6) and high entropy rare earth hexaborides/borates (HE REB6/HE REBO3) composite powders, J. Adv. Ceram. (2020).
[34] W. Zhang, B. Zhao, N. Ni, H. Xiang, F.-Z. Dai, S. Wu, Y. Zhou, High entropy rare earth hexaborides/tetraborides (HE REB6/HE REB4) composite powders with enhanced electromagnetic wave absorption performance, J. Mater. Sci. Technol. 87 (2021) 155–166.
[35] H. Bergmann, G. Czack, H. Hein, S. Ruprecht, U. Vetter, Rare earth elements and boron, in: H. Hein, C. Koeppel, U. Vetter, E. Warkentin, H. Bergmann, G. Czack, H. Hein, S. Ruprecht, U. Vetter (Eds.), Sc, Y, La-Lu, Rare Earth Elements: Compounds With Boron, Springer Berlin Heidelberg, Berlin, Heidelberg, 1989, pp. 1–273.
[36] K.E. Spear, Rare earth-boron phase equilibria, in: V.I. Matkovich (Ed.), Boron and Refractory Borides, Springer Berlin Heidelberg, Berlin, Heidelberg, 1977, pp. 439–456.
[37] A.V. Matovnikov, V.S. Urbanovich, T.A. Chukina, A.A. Sidorov, V.V. Novikov, Two-step syntheses of rare-earth diborides, Inorg. Mater. 45 (4) (2009) 366–368.
[38] V.V. Novikov, A.V. Matovnikov, O.S. Volkova, N. Vasil'ev, Synthesis, thermal and magnetic properties of RE-diborides, J. Mag. Mag. Mater. 428 (2017) 239–245.
[39] G. Tallarita, R. Licheri, S. Garroni, R. Orrù, G. Cao, Novel processing route for the fabrication of bulk high-entropy metal diborides, Scripta Mater. 158 (2019) 100–104.
[40] D. Liu, H. Liu, S. Ning, B. Ye, Y. Chu, Synthesis of high-purity high-entropy metal diboride powders by boro/carbothermal reduction, J. Am. Ceram. Soc. 102 (12) (2019) 7071–7076.
[41] H. Klesnar, P.F. Rogl, Phase relations in the ternary systems rare-earth metal (RE)-boron-nitrogen, where RE=Tb, Dy, Ho, Er, Tm, Lu, Sc, and Y, High Temp. High Pressure 22 (1990) 453–457.
[42] Y.-C. Huang, Z.-B. Xiao, Y. Liu, Crystallography of Zr poisoning of Al - Ti - B grain refinement using edge-to-edge matching model, J. Central South Univ. (English Edition) 20 (10) (2013) 2635–2642.
[43] B. Lönnberg, Thermal expansion studies on the group IV–VII transition metal diborides, J. Less Common Metals 141 (1) (1988) 145–156.
[44] L. Feng, F. Monteverde, W.G. Fahrenholtz, G.E. Hilmas, Superhard high-entropy AlB2-type diboride ceramics, Scripta Mater. 199 (2021), 113855.

[45] Y. Zhang, S.-K. Sun, W.-M. Guo, W. Zhang, L. Xu, J.-H. Yuan, D.-K. Guan, D.-W. Wang, Y. You, H.-T. Lin, Fabrication of textured (Hf0.2Zr0.2Ta0.2Cr0.2Ti0.2)B2 high-entropy ceramics, J. Eur. Ceram. Soc. 41 (1) (2021) 1015–1019.
[46] J. Schmidt, M. Boehling, U. Burkhardt, Y. Grin, Preparation of titanium diboride TiB2 by spark plasma sintering at slow heating rate, Sci. Technol. Adv. Mater. 8 (5) (2007) 376–382.
[47] S. Ran, L. Zhang, O. Van der Biest, J. Vleugels, Pulsed electric current, in situ synthesis and sintering of textured TiB2 ceramics, J. Eur. Ceram. Soc. 30 (4) (2010) 1043–1047.
[48] W.D. Nix, H. Gao, Indentation size effects in crystalline materials: a law for strain gradient plasticity, J. Mech. Phys. Solids 46 (3) (1998) 411–425.
[49] R.W. Rice, Porosity dependence of hardness, compressive strength porosity dependence of hardness, compressive strength, wear, and related behavior At 22° C. Porosity of Ceramics, CRC Press, 2017, pp. 276–314.
[50] J.C. LaSalvia, L.W. Meyer, M.A. Meyers, Densification of reaction-synthesized titanium carbide by high-velocity forging, J. Am. Ceram. Soc. 75 (3) (1992) 592–602.
[51] O. Yamada, Y. Miyamoto, M. Koizumi, High-pressure self-combustion sintering of titanium carbide, J. Am. Ceram. Soc. 70 (9) (1987). C-206-C-208.
[52] R.W. Rice, C.C. Wu, F. Boichelt, Hardness–grain-size relations in ceramics, J. Am. Ceram. Soc. 77 (10) (1994) 2539–2553.
[53] A. Zaoui, S.A. Abderrahmane, M. Djermouni, S. Kacimi, F. Zazoua, A. Boukortt, M. Bejar, E. Dhahri, Hardness in rare earth diboride systems: Ab initio full-potential study, Superlattices Microstruct. 101 (2017) 575–583.
[54] H. Ozisik, E. Deligoz, K. Colakoglu, G. Surucu, Structural and mechanical stability of rare-earth diborides, Chin. Phys. B 22 (4) (2013), 046202.
[55] A. Jain, S.P. Ong, G. Hautier, W. Chen, W.D. Richards, S. Dacek, S. Cholia, D. Gunter, D. Skinner, G. Ceder, K.A. Persson, Commentary: the Materials Project: a materials genome approach to accelerating materials innovation, APL, Materials 1 (1) (2013), 011002.
[56] C. Wang, M. Qin, T. Lei, Y. He, K. Kisslinger, T.J. Rupert, J. Luo, H.L. Xin, Synergic grain boundary segregation and precipitation in W- and W-Mo-containing high-entropy borides, J. Eur. Ceram. Soc. 41 (10) (2021) 5380–5387.
[57] Z. Zhang, S. Zhu, F.-Z. Dai, H. Xiang, Y. Liu, L. Liu, Z. Ma, S. Wu, F. Liu, K. Sun, Y. Zhou, Theoretical predictions and experimental verification on the phase stability of enthalpy-stabilized HE TMREB2s, J. Mater. Sci. Technol. 121 (2022) 154–162.
[58] Z. Zhang, S. Zhu, Y. Liu, L. Liu, Z. Ma, Enthalpy driving force and chemical bond weakening: The solid-solution formation mechanism and densification behavior of high-entropy diborides (Hf1−x/4Zr1−x/4Nb1−x/4Ta1−x/4Scx)B2, J. Eur. Ceram. Soc. (2022).
[59] L. Backman, J. Gild, J. Luo, E.J. Opila, Part II: experimental verification of computationally predicted preferential oxidation of refractory high entropy ultra-high temperature ceramics, Acta Mater. 197 (2020) 81–90.